Invited Paper

Frequency domain modeling of nanophotonic devices

Georgios Veronis and Shanhui Fan

Department of Electrical Engineering, Stanford University, Stanford, California 94305

ABSTRACT

Several problems in nanophotonics are uniquely suitable for frequency domain modeling methods. We first present a new method for sensitivity analysis of nanophotonic devices. The algorithm is based on the finite-difference frequency-domain method and uses the adjoint variable method and perturbation theory techniques. We show that our method is highly efficient and accurate and can be applied to the calculation of the sensitivity of transmission parameters of resonant nanophotonic devices. Frequency-domain methods are also essential in modeling of plasmonic devices due to the complicated dispersion properties of metals at optical frequencies. Here we demonstrate the existence of a bound optical mode supported by a slot in a thin metallic film deposited on a substrate, with slot dimensions much smaller than the wavelength. The modal size is almost completely dominated by the near field of the slot. Consequently, the size is very small compared with the wavelength, even when the dispersion relation of the mode approaches the light line of the surrounding media. In addition, the group velocity of this mode is close to the speed of light in the substrate, and its propagation length is tens of microns at the optical communication wavelength.

Keywords: Sensitivity analysis, photonic crystals, plasmonic devices

1. INTRODUCTION

Several problems in nanophotonics are uniquely suitable for frequency domain modeling methods.

Here we first present a highly accurate and efficient method for sensitivity analysis of nanophotonic devices. The algorithm is based on the finite-difference frequency-domain method and uses the adjoint variable method and perturbation theory techniques. We show that this method can also be applied to the calculation of the sensitivity of transmission parameters of resonant nanophotonic devices. We also note that this method is uniquely suitable for frequency domain simulations, as discussed below.

In addition, the dielectric constant of metals at optical wavelengths is complex, i.e. $\epsilon_r(\omega) = \epsilon_{\mathrm{Re}}(\omega) + i\epsilon_{\mathrm{Im}}(\omega)$ and is a complicated function of frequency.[1] Thus, several simulation techniques which are limited to lossless, non-dispersive materials are not applicable to plasmonic devices. In time-domain methods the dispersion properties of metals have to be approximated by suitable analytical expressions.[2] In most cases the Drude model is invoked to characterize the frequency dependence of the metallic dielectric function[3]

$$\epsilon_{r,\mathrm{Drude}} = 1 - \frac{\omega_p^2}{\omega(\omega + i\gamma)} \tag{1}$$

where ω_p, γ are frequency-independent parameters. However, the Drude model approximation is valid over a limited wavelength range. The range of validity of the Drude model can be extended by adding Lorentzian terms to Eq. (1) to obtain the Lorentz-Drude model[3]

$$\epsilon_{r,\mathrm{LD}} = \epsilon_{r,\mathrm{Drude}} + \sum_{j=1}^{k} \frac{f_j \omega_j^2}{(\omega_j^2 - \omega^2) - i\omega\gamma_j} \tag{2}$$

where ω_j and γ_j stand for the oscillator resonant frequencies and bandwidths respectively, and f_j are weighting factors. Physically, the Drude and Lorentzian terms are related to intraband (free-electron) and interband (bound-electron) transitions respectively.[3] Even though the Lorentz-Drude model extends the range of validity of analytical approximations to metallic dielectric constants, it is not suitable for description of sharp absorption edges observed in some metals, unless a very large number of terms is used. In particular, the Lorenz-Drude model cannot approximate well the onset of interband absorption in noble metals (Ag, Au, Cu) even if five

Photonics: Design, Technology, and Packaging II, edited by Derek Abbott, Yuri S. Kivshar, Halina H. Rubinsztein-Dunlop, Shanhui Fan, Proc. of SPIE Vol. 6038, 60380X, (2006) · 0277-786X/06/$15 · doi: 10.1117/12.651341

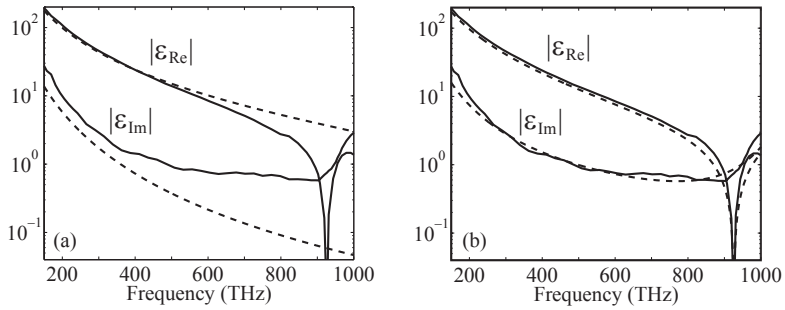

Figure 1. Real and imaginary part of the dielectric constant of silver at optical frequencies. The solid lines show experimental data. The dashed lines show values calculated using (a) the Drude model, (b) the Lorentz-Drude model with five Lorentzian terms. The parameters of the models are optimal and obtained through an optimization procedure.

Lorentzian terms are used.[3] In Fig. 1 we compare the Drude and Lorentz-Drude models with experimental data for silver. We observe that even a five-term Lorentz-Drude model with optimal parameters results in a factor of two error at certain frequencies. As a result, broadband time-domain simulations can give accurate results in a limited wavelength range. Frequency-domain techniques are more suitable for modeling of plasmonic metallic devices, since they can treat arbitrary material dispersion. Here we demonstrate the existence of a bound plasmonic mode supported by a slot in a thin metallic film deposited on a substrate, with slot dimensions much smaller than the wavelength.

2. SENSITIVITY ANALYSIS OF NANOPHOTONIC DEVICES

For practical implementations of photonic crystal devices, it is of fundamental importance to determine the sensitivity of the device properties to fabrication-related disorders.[4–8] In principle, the sensitivity can be determined by varying the device parameters in the vicinity of the design point, and by calculating the response functions of the resulting perturbed devices. However, such a direct approach is computationally inefficient, since it requires a full analysis for each variation of the design parameters. Moreover, in practice it is important to determine the sensitivity with respect to variations of geometrical parameters. In the commonly-used finite-difference time-domain (FDTD) method, a variation of the device size by a single grid point may already lead to large structural change. Consequently, in order to determine the sensitivity accurately in the direct approach, a high-resolution grid is typically needed, further increasing the computational cost.

Here we introduce a new approach for sensitivity analysis of photonic crystal structures based upon the adjoint variable method[9] (AVM) and perturbation theory in a frequency-domain solver for Maxwell's equations. In this approach, once a simulation for the device properties is performed, the sensitivity with respect to any number of design parameters is calculated with very small additional computational cost. Furthermore, this approach determines the sensitivity with respect to geometrical parameter variations accurately without the need for the use of high-resolution grids. We expect this approach to be important for fast computational prototyping of practical photonic crystal and nanophotonic devices.

2.1. Formulation

In frequency-domain, the wave equation for the electric field is

$$[-\nabla \times \nabla \times + k_0^2 \epsilon_r]\mathbf{E} = \nabla \times \mathbf{M} + j\omega\mu_0\mathbf{J} \tag{3}$$

where $k_0^2 = \omega^2\epsilon_0\mu_0$ and $\mathbf{J}$ ($\mathbf{M}$) is the electric (magnetic) source current. To solve this equation, we use a finite-difference frequency-domain (FDFD) method.[10] The fields are discretized on a nonuniform orthogonal grid truncated by a perfectly matched layer (PML) in its coordinate stretching formulation.[11] The spatial discretization of Eq. (3) on the grid results in a system of complex linear equations. The equation for the field at each grid point involves only the fields at the six (four in 2-D) adjacent grid points. Thus the resulting system matrix is sparse.

The system of linear equations resulting from discretizing Eq. (3) is of the general form

$$\mathbf{Z}(\mathbf{s})\mathbf{I} = \mathbf{V} \tag{4}$$

where $\mathbf{Z}$ is the system matrix, $\mathbf{s}$ is the vector of design parameters, $\mathbf{I}$ is the vector of unknown fields, and $\mathbf{V}$ is the source which does not depend on $\mathbf{s}$ ($\nabla_s \mathbf{V} = 0$), since we focus on variations of the device structure. The response function of interest is a function of the field $T = T(\mathbf{I}(\mathbf{s}))$ and therefore has no explicit dependence on $\mathbf{s}$. The objective of the sensitivity analysis is to determine the gradient of the response function with respect to the design parameters $\nabla_s T$. Using AVM, it can be shown that[9]

$$\nabla_s T = -\hat{\mathbf{I}}^T (\nabla_s \mathbf{Z})\mathbf{I} \tag{5}$$

$$\mathbf{Z}^T \hat{\mathbf{I}} = [\nabla_{\mathbf{I}} T]^T \tag{6}$$

where $\mathbf{I}$, obtained from Eq. (4), is the vector of fields at the current design point, and $\hat{\mathbf{I}}$ is the solution to the so-called *adjoint problem* (Eq. (6)). In our case, the matrix $\mathbf{Z}$ obtained from Eq. (3) is symmetric. Thus, Eq. (6) requires determining the field when the source is the *adjoint excitation* $\hat{\mathbf{V}} = [\nabla_{\mathbf{I}} T]^T$, which is the gradient of the response with respect to the fields. As an example, if the response function is defined as the field intensity at a given monitor point, the adjoint excitation will be nonzero only at the monitor point.

In summary, sensitivity analysis using the adjoint variable method consists of three steps. First, the electromagnetic fields $\mathbf{I}$ at a specific design point are calculated by solving Eq. (4). Second, the adjoint problem is solved (Eq. (6)). In the adjoint problem the device structure is unperturbed but the source is the adjoint excitation, which is nonzero only at the monitor points. Once the field $\mathbf{I}$ and the adjoint field $\hat{\mathbf{I}}$ are calculated, the sensisitivity is obtained by the summation in Eq. (5). In the case of sensitivity analysis with respect to fabrication disorders, this summation has to be carefully considered, as discussed below. If we are interested in the sensitivity with respect to many different design parameters we only need to solve Eqs. (4) and (6) once. For each design parameter the sensitivity is then obtained through Eq. (5).

A particularly efficient approach to solve Eqs. (4) and (6) is the use of a direct sparse matrix method, which requires only a single LU decomposition of $\mathbf{Z}$ and two back-substitutions. Having calculated $\mathbf{I}$ and $\hat{\mathbf{I}}$, the sensitivity with respect to *any* number of design parameters is obtained by calculating $\nabla_s \mathbf{Z}$ which has a negligible computational cost. Thus, when a direct solver is used, the only additional cost required for the sensitivity analysis is one back-substitution for the solution of Eq. (6), which is typically at least an order of magnitude smaller than the cost of the LU decomposition.

In the device sensitivity analysis, we are interested in the effects of variations of the dielectric function $\epsilon_r = \epsilon_r(\mathbf{r})$ on the response function of the device. To calculate the effect of varying the dielectric constant ϵ_{r1} of a particular device (assuming that the entire device region has the same dielectric constant ϵ_{r1}), it is straightforward to calculate $\nabla_s \mathbf{Z}$, and then, using Eq. (5), one obtains

$$\frac{\partial T}{\partial \epsilon_{r1}} = -k_0^2 \sum_i \hat{I}_i I_i \tag{7}$$

where the summation is taken over the volume of this device.

In practice, it is particularly useful to determine the tolerance of the device performance to fabrication disorders. In this case, we are interested in the effect of perturbations due to shifting of the interface between regions with different dielectric constants. Suppose we have two regions with dielectric constants ϵ_{r1} and ϵ_{r2}. Since $\epsilon_r(\mathbf{r})$ is a step function, its derivative is a delta function, so that the summation in Eq. (5) is limited to the interface between the two media. This surface summation needs to be carefully defined, due to the discontinuity of the normal component of the electric field $E_\perp$ to the interface, and has recently been studied by Johnson *et al.*[12] in the context of perturbation theory. Following their approach, we showed that

$$\frac{\partial T}{\partial s} = -k_0^2 \sum_i \Delta l_i^{-1} \frac{dh(\mathbf{r}_{\mathrm{surf}i}, s)}{ds} [\Delta\epsilon_{12} \hat{E}_{\parallel i} E_{\parallel i} - \Delta(\epsilon_{12}^{-1}) \hat{D}_{\perp i} D_{\perp i}] \tag{8}$$

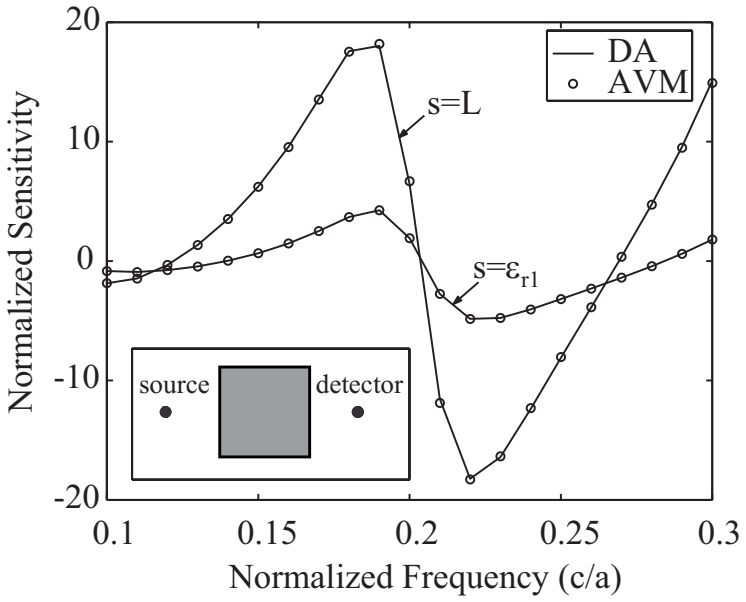

Figure 2. Comparison of the DA and AVM methods in high-resolution grids (160 points per a). We show the normalized sensitivity of the transmission defined as $\frac{\partial T}{\partial s}(\frac{T}{s})^{-1}$ (s is either the square size L or ϵ_{r1}) as a function of frequency. The structure, a dielectric block, is shown in the inset and L =0.9375a, ϵ_{r1} =11.56.

where $\Delta\epsilon_{12} \equiv \epsilon_{r1} - \epsilon_{r2}$, $\Delta(\epsilon_{12}^{-1}) \equiv \epsilon_0^{-2}(\epsilon_{r1}^{-1} - \epsilon_{r2}^{-1})$, Δl_i is the local grid size normal to the interface, and the summation is taken over the interface. The function $h = h(\mathbf{r}_{\rm surf}, s)$ defined on the boundary surface is the distance that the interface between regions 1 and 2 shifts towards region 2. The summation in Eq. (8) is well-defined, since both $E_\parallel$ and $D_\perp$ are continuous at the interface.

We focus on 2-D calculations as a proof of principle. For TE polarization we have $\mathbf{E} = E_z\hat{z}$ and the wave equation for the electric field becomes[11]

$$[\frac{\partial^2}{\partial x^2} + \frac{\partial^2}{\partial y^2} + k_0^2\epsilon_r]E_z = j\omega\mu_0 J_z \tag{9}$$

Similarly, for TM polarization we have $\mathbf{H} = H_z\hat{z}$ and

$$[\frac{\partial}{\partial x}(\frac{1}{\epsilon_r}\frac{\partial}{\partial x}) + \frac{\partial}{\partial y}(\frac{1}{\epsilon_r}\frac{\partial}{\partial y}) + k_0^2]H_z = j\omega\epsilon_0 M_z \tag{10}$$

In the TM case, $\mathbf{I}$ and $\hat{\mathbf{I}}$ correspond to magnetic fields. To use Eq. (8) where the sensitivity is calculated in terms of the electric field, we first solve Eq. (10) to determine H_z, from which $E_\parallel$ and $D_\perp$ can then be calculated. The adjoint problem can also be recast in terms of the magnetic field. If the response function is defined as $T = |H_{\rm obs}|^2$ where $H_{\rm obs}$ is the field at the observation point, we can show that the adjoint source is $\hat{M}_z = -\frac{2}{j\omega\mu_0}H^*_{\rm obs}$ at the observation point and zero elsewhere.

We also note that sensitivity analysis of nanophotonic devices is uniquely suitable for frequency domain simulations. In principle the sensitivity analysis algorithm presented here could also be used in conjunction with the FDTD method. However, in the FDTD method the calculated fields on the entire perturbed volume or surface have to be transformed to the frequency domain. This can only be done using a computationally expensive on-the-fly Fourier transform to avoid storing all the time samples of the fields over the entire volume or surface. In addition, the FDTD simulation of the adjoint problem has to run backward in time and requires special absorbing boundary conditions. Finally, in sensitivity analysis methods with FDTD the response function is typically expressed as an integral in time. Thus,the sensitivity of device performance to parameter variations

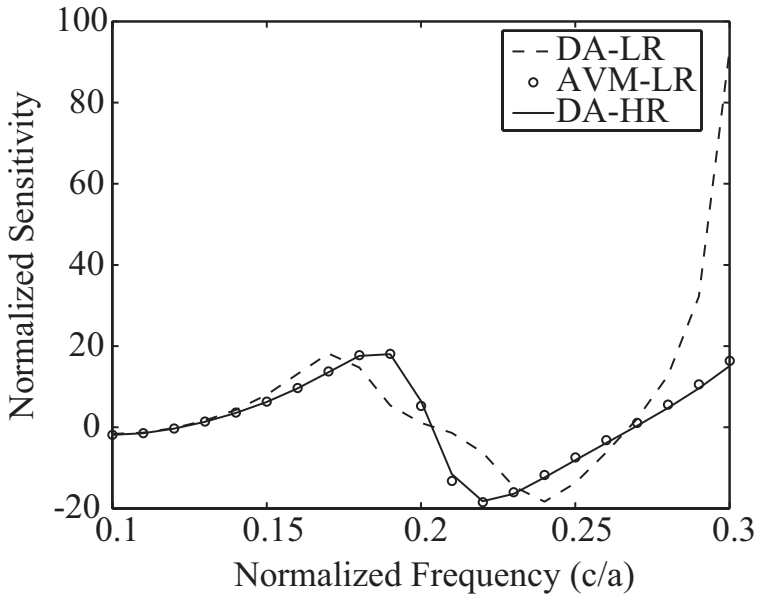

Figure 3. Comparison of the DA and AVM methods in low-resolution grids (16 points per a) with the benchmark DA in high-resolution grid (160 points per a) for $s = L$.

as a function of the operating wavelength, which is of practical interest in photonic devices, is hard to obtain from such formulations.

2.2. Method validation and evaluation

To validate our method, we compare it with the direct approach (DA),[9] in which sensitivity is simply calculated as

$$\frac{\partial T}{\partial s} \simeq \frac{T(s + \Delta s/2) - T(s - \Delta s/2)}{\Delta s} \tag{11}$$

We choose a high-resolution grid (160 points per a, where a is a length used for normalization). In Fig. 2 we show the sensitivity of the response function, calculated with the DA and our method for the structure shown in the inset of Fig. 2. We observe that there is excellent agreement over the entire frequency range.

Since our method uses a perturbative approach for the calculation of sensitivity, we expect it to be accurate even when a low-resolution grid is used. To verify this, we compare our method in a low-resolution grid (16 points per a) to the benchmark DA in the high-resolution grid (160 points per a). Results are shown in Fig. 3 for the sensitivity with respect to the object size. The agreement is very good over the entire frequency range in spite of the 10 times coarser grid. In Fig. 3 we also show the result obtained by the DA in the low-resolution grid. We observe that the DA, when applied to a low-resolution grid, introduces very large error especially at high frequencies.

Our method is significantly more efficient than the DA. The DA requires two full solutions at design points $s+\Delta s/2$ and $s-\Delta s/2$ (including both the LU decomposition and the back-substitution) for *each* design parameter. Thus, for n design parameters a total of $2n + 1$ full analyses are required. Our method, as mentioned above, requires only one additional back-substitution, irrespective of the number of design parameters.

2.3. Sensitivity of transmission parameters of resonant nanophotonic devices

As an application of our method, we calculate the sensitivity of the resonant frequency and the bandwidth of an optical filter. One photonic-crystal band-pass filter geometry[13] is shown in Fig. 4. The transmission spectrum

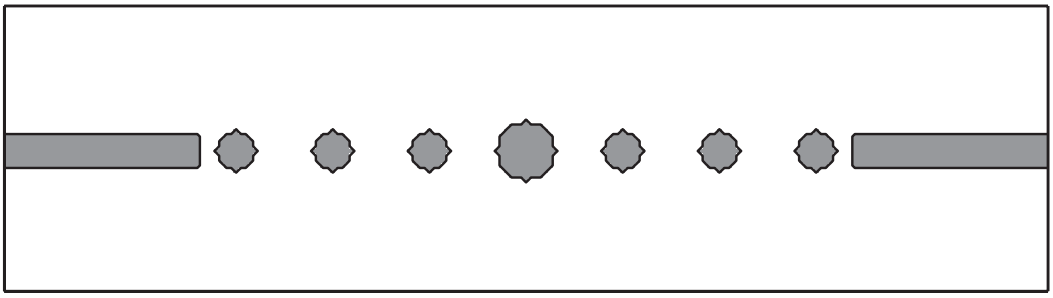

Figure 4. Device geometry of a photonic-crystal band-pass filter.

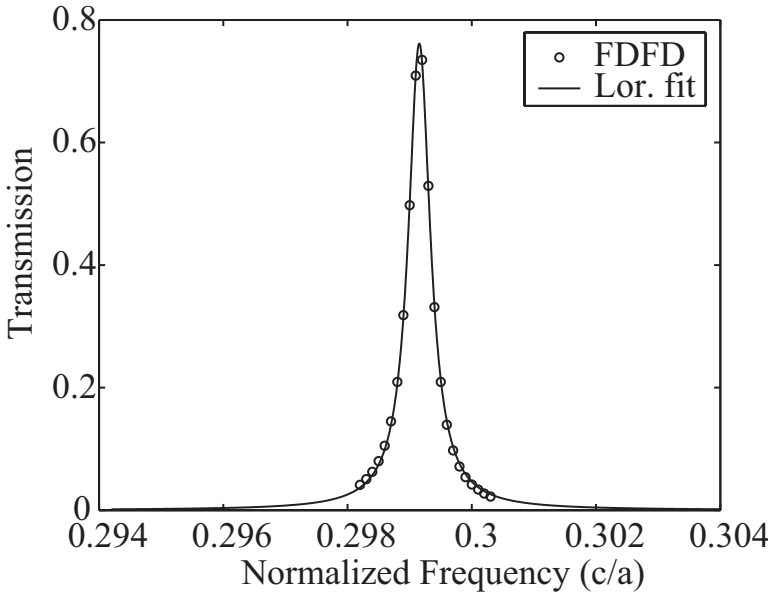

Figure 5. Transmission spectrum calculated by FDFD and the corresponding Lorentzian fit for a photonic-crystal-based band-pass optical filter (the device geometry is shown in Fig. 4). The distance between adjacent rods is a and their radius is $0.2a$. The radius of the central dielectric rod is r_d=$0.4a$. The width of the dielectric waveguides is $0.35a$, and their distance from the center of the closest rod is $0.4a$.

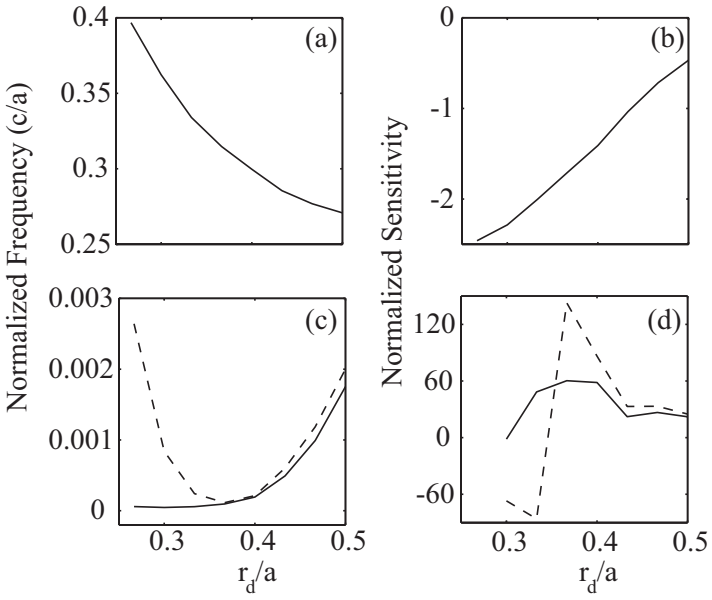

Figure 6. (a) Ω_0, (c) Ω_1, Ω_2 (shown with a dashed line) as a function of the radius of the central dielectric rod r_d. Normalized sensitivities (b) $\frac{\partial\Omega_0}{\partial r_d}(\frac{\Omega_0}{a})^{-1}$, (d) $\frac{\partial\Omega_1}{\partial r_d}(\frac{\Omega_1}{a})^{-1}$, $\frac{\partial\Omega_2}{\partial r_d}(\frac{\Omega_2}{a})^{-1}$ (shown with a dashed line) as a function of r_d.

of such a device close to the resonant frequency can be very well approximated by a Lorentzian shape

$$T(\omega) = \frac{\Omega_1^2}{(\omega - \Omega_0)^2 + {\Omega_2}^2} \tag{12}$$

as shown in Fig. 5, where Ω_0 is the resonant frequency, and Ω_1, Ω_2 are bandwidths.

To calculate $\frac{\partial\Omega_0}{\partial s}$, $\frac{\partial\Omega_1}{\partial s}$, $\frac{\partial\Omega_2}{\partial s}$. we differentiate Eq. (12) to obtain

$$\frac{\partial T(\omega_i)}{\partial s} = \frac{\partial T(\omega_i)}{\partial \Omega_0}\frac{\partial \Omega_0}{\partial s} + \frac{\partial T(\omega_i)}{\partial \Omega_1}\frac{\partial \Omega_1}{\partial s} + \frac{\partial T(\omega_i)}{\partial \Omega_2}\frac{\partial \Omega_2}{\partial s} \tag{13}$$

Here, $\frac{\partial T(\omega_i)}{\partial s}$ is calculated using the method described above. In addition, $\frac{\partial T(\omega_i)}{\partial \Omega_0}$, $\frac{\partial T(\omega_i)}{\partial \Omega_1}$, $\frac{\partial T(\omega_i)}{\partial \Omega_2}$ can be analytically calculated from Eq. (12), once the transmission spectrum is fitted with a Lorentzian. Thus, one can determine $\frac{\partial\Omega_0}{\partial s}$, $\frac{\partial\Omega_1}{\partial s}$, $\frac{\partial\Omega_2}{\partial s}$ if Eq. (13) is applied to a minimum of three frequency points close to Ω_0. In practice, more accurate results are obtained if more than three frequency points are used, and the overdetermined system is solved in the least-squares sense. Alternatively, $\frac{\partial\Omega_0}{\partial s}$, $\frac{\partial\Omega_1}{\partial s}$, $\frac{\partial\Omega_2}{\partial s}$ can be obtained if we differentiate some other function of the transmission spectrum such as T^{-1}

$$-T(\omega_i)^{-2}\frac{\partial T(\omega_i)}{\partial s} = \frac{\partial T(\omega_i)^{-1}}{\partial \Omega_0}\frac{\partial \Omega_0}{\partial s} + \frac{\partial T(\omega_i)^{-1}}{\partial \Omega_1}\frac{\partial \Omega_1}{\partial s} + \frac{\partial T(\omega_i)^{-1}}{\partial \Omega_2}\frac{\partial \Omega_2}{\partial s} \tag{14}$$

Depending on the design point, either Eq. (13) or Eq. (14) results in a better least-squares fit. In each case, we use the one which provides the best fit to our results.

In Figs. 6a, 6c we show the calculated Ω_0, Ω_1, Ω_2 for the device structure of Fig. 4, as a function of the radius of the central dielectric rod r_d. We observe that Ω_0 decreases as r_d increases, and that both Ω_1 and Ω_2 are much smaller than Ω_0 due to the high-Q defect dipole-mode formed by modifying r_d.[13] In Figs. 6b, 6d we show the calculated sensitivities of Ω_0, Ω_1, Ω_2. We observe that Ω_1, Ω_2 are much more sensitive to variations in r_d than Ω_0. The calculated Ω_0, Ω_1, Ω_2 are consistent with previously published results,[13] and their calculated sensitivities are consistent with the values obtained by the DA in the same grid.

3. GUIDED SUBWAVELENGTH PLASMONIC MODE SUPPORTED BY A SLOT IN A THIN METAL FILM

Waveguide structures which support highly-confined optical modes are important for achieving compact integrated photonic devices.[14,15] In particular, plasmonic waveguides have shown the potential to guide subwavelength optical modes. Several different plasmonic waveguiding structures have been proposed.[14,16–25] However, these structures support a highly-confined mode only near the surface plasmon frequency. In this regime, the optical mode typically has low group velocity and short propagation length.

Here we investigate the characteristics of the bound optical mode supported by an air slot in a thin metallic film deposited on a substrate (inset of Fig. 7a). This structure is hereafter referred to as a plasmonic slotline. Of particular interest is the regime where the dimensions of the slot are much smaller than the wavelength. We show that such a structure supports a fundamental bound mode with size almost completely dominated by the near field of the slot over a wide range of frequencies. The size of this mode can be far smaller than the wavelength even when its effective index approaches that of the substrate. In addition, the group velocity of the mode is close to the speed of light in the substrate and its propagation length is tens of microns at the optical communication wavelength. Thus, such a waveguide could be potentially important in providing an interface between conventional optics and subwavelength electronic and optoelectronic devices.

3.1. Finite-difference frequency-domain mode solver

We calculate the eigenmodes of the plasmonic slotline at a given wavelength λ_0 using a full-vectorial FDFD mode solver. For waveguiding structures which are uniform in the z direction, if an $\exp(-\gamma z)$ dependence is assumed for all field components, Maxwell's equations reduce to two coupled equations for the transverse magnetic field components H_x and H_y.[26] These equations are discretized on a non-uniform orthogonal grid resulting in a sparse matrix eigenvalue problem of the form $\mathbf{Ah} = \gamma^2\mathbf{h}$, which is solved using iterative sparse eigenvalue techniques.[11] To calculate the bound eigenmodes of the waveguide, we ensure that the size of the computational domain is large enough so that the fields are negligibly small at its boundaries,[27] while for leaky modes we use perfectly matched layer absorbing boundary conditions.[11] An important feature of this formulation is the absence of spurious modes.[27] In addition, the frequency-domain mode solver allows us to directly use experimental data for the frequency-dependent dielectric constant of metals,[1] including both the real and imaginary parts, with no further approximation. We define here the propagation length L_p and the effective index n_eff of a propagating mode through the equation $\gamma \equiv L_\mathrm{p}^{-1} + i\beta = L_\mathrm{p}^{-1} + i2\pi n_\mathrm{eff}\lambda_0^{-1}$.

3.2. Dispersion relation of the plasmonic slotline mode

In Fig. 7a we show the dispersion relation of the fundamental mode of the plasmonic slotline. The width w and thickness t of the slot are 50 nm and the substrate material is silica (n_s =1.44). We observe that such a structure supports a bound mode in a wide frequency range. Within this range this mode has a wavevector larger than all radiation modes in air and silica, as well as all propagating modes in the air-silver-silica thin film structure. The cutoff frequency of this mode is $\sim 0.005(2\pi c/w)$, where c is the speed of light in free space. We also found that, if the slot dimensions are smaller than 100 nm, the optical communication frequency (λ_0 =1.55μm) is well above ω_cutoff. Since the slot dimensions are much smaller than the wavelength in the frequency range of interest, the fundamental bound mode is quasi-TEM with dominant field components E_x and H_y, and this waveguide does not support any higher order bound modes. Since the fundamental mode is quasi-TEM, it can be efficiently excited by linearly polarized light.

As a comparison, in Fig. 7a we also show the dispersion relation when the perfect electric conductor (PEC) approximation is used for the metallic regions. We observe that the PEC slotline structure on substrate does not support a bound mode at any frequency. When the slot dimensions are far smaller than the wavelength, the fields are essentially the same as those of the static case.[28] In the PEC case, the fields do not penetrate into the metal. The field lines are either in air or in silica. The effective index of the mode n_eff therefore satisfies the relation $1 < n_\mathrm{eff} < n_s$.[28] The PEC model is commonly used to describe slotlines at microwave frequencies. While such structures do not support any bound mode, in practice they guide waves effectively,[28,29] since radiation loss turns out to be negligible for deep subwavelength structures. In comparison, the existence of a bound mode for

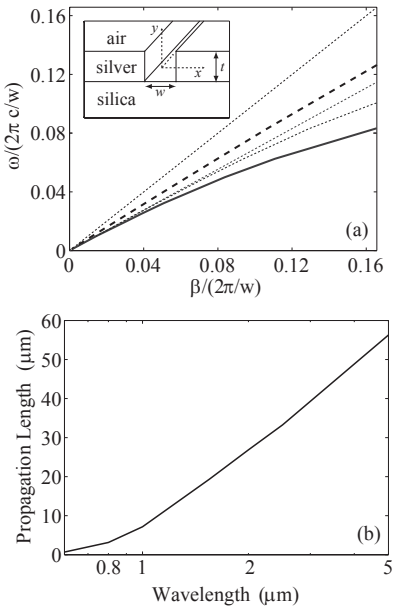

Figure 7. (a) Dispersion relation of the fundamental mode of the plasmonic slotline (shown with solid line) for w, t =50 nm (see inset) and of a PEC slotline (shown with dashed line). The upper, middle, and lower thin dotted curves are the light lines of air and silica and the lowest frequency mode of the silver film, respectively. (b) Propagation length of the fundamental mode of the plasmonic slotline as a function of wavelength for w, t =50 nm.

the plasmonic slotline is entirely due to the finite negative dielectric constant of metals at optical frequencies, which results in higher n_{eff} for the fundamental mode.

In Fig. 7b we show the propagation length L_{p} of the fundamental mode of the plasmonic slotline as a function of wavelength. The propagation length decreases as the wavelength decreases. This is due to the fact that the propagation length of surface plasmons scales with the wavelength,[30] since the fraction of the modal power in the metal increases at shorter wavelengths,[19] and also due to increased material losses of metals at shorter wavelengths.[1] At the optical communication wavelength of 1.55μm the propagation length is $\sim$20μm.

3.3. Modal size

In Fig. 8a we show the power density profile of the fundamental mode of the plasmonic slotline for λ_0 =1.55μm. We observe that the mode is mostly confined in the slot region and slightly extends in the adjacent silica and air regions. The maximum intensity is observed at the silver-air interfaces in the slot. This is expected since the mode can be seen as being formed by the coupling of the surface plasmon-polaritons at the two silver-air interfaces. In Fig. 8b we show the modal size, defined as the square root of the area in which the mode power density is larger than $1/e^2$ of its maximum value, as a function of frequency. At the optical communication wavelength of 1.55μm the modal size is $\sim$87 nm, which is much smaller than the minimum achievable modal sizes with high-index-contrast dielectric waveguides. For comparison, the minimum achievable modal size with square silicon waveguides embedded in silica at λ_0 =1.55μm is $\sim$400 nm.[31] We also note that the modal size varies only weakly as a function of frequency.

We observe that the modal size remains small even at low frequencies where the dispersion relation approaches the silica light line. This behavior is fundamentally different from that of conventional dielectric waveguides. In conventional dielectric waveguides, the fields in the low-index cladding surrounding the high-index core decay exponentially with a decay constant $\alpha = \frac{2\pi}{\lambda_0}\sqrt{n_{\text{eff}}^2 - n_{\text{clad}}^2}$, where n_{clad} is the refractive index of the cladding region.[32] In these structures, the minimum confinement of a guided optical mode is $\sim \lambda_0/(2n_{\text{core}})$, where n_{core} is the refractive index of the core region.[14] If the dimensions of the core are reduced far below $\lambda_0/(2n_{\text{core}})$, the dispersion relation of the optical mode approaches the cladding light line ($n_{\text{eff}} \rightarrow n_{\text{clad}}$), the decay constant

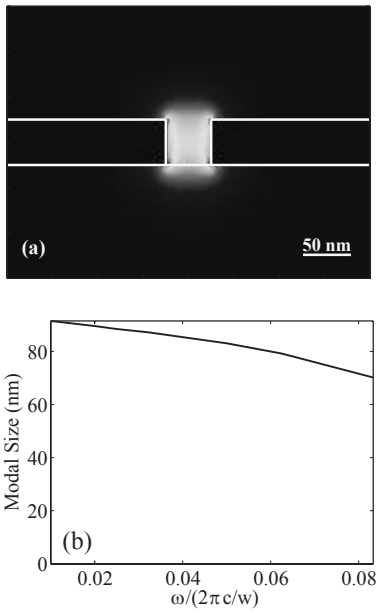

Figure 8. (a) Power density profile at λ_0 =1.55μm, and (b) Modal size as a function of frequency of the fundamental mode of the plasmonic slotline for w, t =50 nm.

α becomes extremely small, and the modal size becomes extremely large.[31, 32] In contrast, in the case of the plasmonic slotline, even though the same exponential behavior should still hold in the far field, the modal size is dominated by the near field of the slot.

3.4. Near and far field characteristics of the plasmonic slotline mode

In Fig. 9a we show the power density profile of the fundamental mode of the plasmonic slotline in a vertical cut at x =0 (Fig. 7a) for w, t =25nm, 50nm, 100nm and λ_0 =1.55μm. This profile has two distinctive characteristics related to the near and far fields. Far from the slot, the modal power density decays asymptotically as $\sim \exp(-2\alpha\rho)/\rho$, where $\alpha = \mathrm{Re}\sqrt{-\gamma^2 - (\frac{2\pi n_{\mathrm{clad}}}{\lambda_0})^2}$, as expected from Maxwell's equations. If the slot dimensions w, t increase, the effective index of the mode n_{eff} decreases, and therefore, the decay rate α decreases. Note also that, since n_s =1.44>1, the decay rate is always larger in air.

In Fig. 9b we show the power density profile in the vicinity of the slot. We observe that the near field of the slot scales with the slot dimensions w, t and is independent of w/λ_0. This is due to the fact that the slot dimensions are much smaller than the wavelength. In addition, silver satisfies the condition $|\epsilon_{\mathrm{metal}}| \gg \epsilon_{\mathrm{air}}$ at $\lambda_0 \sim$1.55μm.[1] Thus, based on the boundary condition for the normal component of the electric field E_x at the silver-air interfaces in the slot, we have $|E_{x\,\mathrm{metal}}| \ll |E_{x\,\mathrm{air}}|$. The modal profile is therefore highly-confined in the slot region (Fig. 8a) and the modal size is dominated by the near field of the slot. Thus, even when the dispersion relation of the mode approaches the silica light line and the far-field decay rate α decreases, the modal size remains relatively small (Fig. 8b). In addition, since the near field scales with the slot dimensions, the modal size of the plasmonic slotline can be further reduced, if the slot dimensions are reduced. We note that this comes at the cost of reduced propagation length.[33]

ACKNOWLEDGMENTS

This research was supported by DARPA/MARCO under the Interconnect Focus Center and by AFOSR grant FA 9550-04-1-0437.

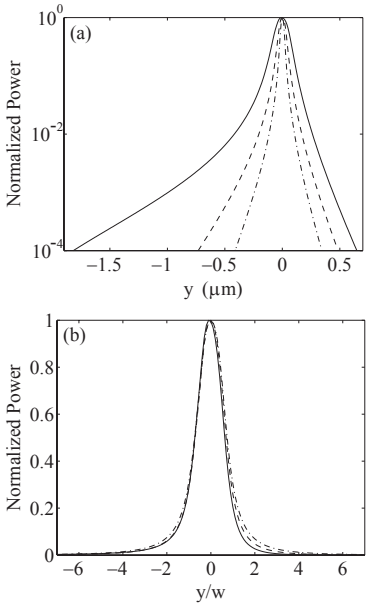

Figure 9. (a) Power density profile at λ_0 =1.55μm of the fundamental mode of the plasmonic slotline at x =0 (Fig. 7a) for w, t =25nm, 50nm, 100nm (shown with dash-dotted, dashed, and solid lines respectively). (b) Power density profile at x =0 in the vicinity of the slot for w, t =25nm, 50nm, 100nm. Note that the horizontal axis is normalized with respect to w.

REFERENCES

1. E. D. Palik, *Handbook of Optical Constants of Solids*, Academic, New York, 1985.
2. A. Taflove, *Computational Electrodynamics*, Artech House, Boston, 1995.
3. A. D. Rakic, A. B. Djurisic, J. M. Elazar, and M. L. Majewski, "Optical properties of metallic films for vertical-cavity optoelectronic devices," *Appl. Opt.* **37**, pp. 5271–5283, 1998.
4. K.-C. Kwan, X. Zhang, Z.-Q. Zhang, and C. T. Chan, "Effects due to disorder on photonic crystal-based waveguides," *Appl. Phys. Lett.* **82**, pp. 4414–4416, 2003.
5. A. Chutinan and S. Noda, "Effects of structural fluctuations on the photonic bandgap during fabrication of a photonic crystal," *J. Opt. Soc. Am. B* **16**, pp. 240–244, 1999.
6. Z.-Y. Li and Z.-Q. Zhang, "Fragility of photonic band gaps in inverse-opal photonic crystals," *Phys. Rev. B* **62**, pp. 1516–1519, 2000.
7. A. A. Asatryan, P. A. Robinson, L. C. Botten, R. C. McPhedran, N. A. Nicorovici, and C. M. de Sterke, "Effects of geometric and refractive index disorder on wave propagation in two-dimensional photonic crystals," *Phys. Rev. E* **62**, pp. 5711–5720, 2000.
8. S. Fan, P. R. Villeneuve, and J. D. Joannopoulos, "Theoretical investigation of fabrication-related disorder on the properties of photonic crystals," *J. Appl. Phys.* **78**, pp. 1415–1418, 1995.
9. N. K. Georgieva, S. Glavic, M. H. Bakr, and J. W. Bandler, "Feasible adjoint sensitivity technique for EM design optimization," *IEEE Trans. Microwave Theory Tech.* **50**, pp. 2751–2758, 2002.
10. S. D. Wu and E. N. Glytsis, "Finite-number-of-periods holographic gratings with finite-width incident beams: analysis using the finite-difference frequency-domain method," *J. Opt. Soc. Am. A* **19**, pp. 2018–2029, 2002.
11. J. Jin, *The Finite Element Method in Electromagnetics*, John Wiley & Sons, New York, 2002.
12. S. G. Johnson, M. Ibanescu, M. A. Skorobogatiy, O. Weisberg, J. D. Joannopoulos, and Y. Fink, "Perturbation theory for Maxwell's equations with shifting material boundaries," *Phys. Rev. E* **65**, pp. 066611/1–7, 2002.
13. S. G. Johnson, S. Fan, A. Mekis, and J. D. Joannopoulos, "Multipole-cancellation mechanism for high-Q cavities in the absence of a complete photonic band gap," *Appl. Phys. Lett.* **78**, pp. 3388–3390, 2001.

14. J. Takahara, S. Yamagishi, H. Taki, A. Morimoto, and T. Kobayashi, "Guiding of a one-dimensional optical beam with nanometer diameter," *Opt. Lett.* **22**, pp. 475–477, 1997.
15. V. R. Almeida, Q. F. Xu, C. A. Barrios, and M. Lipson, "Guiding and confining light in void nanostructure," *Opt. Lett.* **29**, pp. 1209–1211, 2004.
16. J. J. Burke, G. I. Stegeman, and T. Tamir, "Surface-polariton-like waves guided by thin, lossy metal films," *Phys. Rev. B* **33**, pp. 5186–5201, 1986.
17. J. C. Weeber, A. Dereux, C. Girard, J. R. Krenn, and J. P. Goudonnet, "Plasmon polaritons of metallic nanowires for controlling submicron propagation of light," *Phys. Rev. B* **60**, pp. 9061–9068, 1999.
18. J. R. Krenn, B. Lamprecht, H. Ditlbacher, G. Schider, M. Salerno, A. Leitner, and F. R. Aussenegg, "Non-diffraction-limited light transport by gold nanowires," *Europhys. Lett.* **60**, pp. 663–669, 2002.
19. P. Berini, "Plasmon-polariton waves guided by thin lossy metal films of finite width: Bound modes of symmetric structures," *Phys. Rev. B* **61**, pp. 10484–10503, 2000.
20. M. L. Brongersma, J. W. Hartman, and H. A. Atwater, "Electromagnetic energy transfer and switching in nanoparticle chain arrays below the diffraction limit," *Phys. Rev. B* **62**, pp. R16356–R16359, 2000.
21. S. A. Maier, P. G. Kik, H. A. Atwater, S. Meltzer, E. Harel, B. E. Koel, and A. A. G. Requicha, "Local detection of electromagnetic energy transport below the diffraction limit in metal nanoparticle plasmon waveguides," *Nat. Mater.* **2**, pp. 229–232, 2003.
22. F. Kusunoki, T. Yotsuya, J. Takahara, and T. Kobayashi, "Propagation properties of guided waves in index-guided two-dimensional optical waveguides," *Appl. Phys. Lett.* **86**, p. 211101, 2005.
23. K. Tanaka and M. Tanaka, "Simulations of nanometric optical circuits based on surface plasmon polariton gap waveguide," *Appl. Phys. Lett.* **82**, pp. 1158–1160, 2003.
24. I. V. Novikov and A. A. Maradudin, "Channel polaritons," *Phys. Rev. B* **66**, pp. 035403–035413, 2002.
25. D. F. P. Pile and D. K. Gramotnev, "Channel plasmon-polariton in a triangular groove on a metal surface," *Opt. Lett.* **29**, pp. 1069–1071, 2004.
26. J. A. Pereda, A. Vegas, and A. Prieto, "An improved compact 2d full-wave fdfd method for general guided wave structures," *Microwave Opt. Tech. Lett.* **38**, pp. 331–335, 2003.
27. S. J. Al-Bader, "Optical transmission on metallic wires-fundamental modes," *IEEE J. Quantum Electron.* **40**, pp. 325–329, 2004.
28. D. M. Pozar, *Microwave Engineering*, Wiley, New York, 1998.
29. E. A. Mariani, C. P. Heinzman, J. P. Agrios, and S. B. Cohn, "Slot line characteristics," *IEEE Trans. Microwave Theory Tech.* **17**, pp. 1091–1096, 1969.
30. W. L. Barnes, A. Dereux, and T. W. Ebbesen, "Surface plasmon subwavelength optics," *Nature* **424**, pp. 824–830, 2003.
31. L. Vivien, S. Laval, E. Cassan, X. L. Roux, and D. Pascal, "2-d taper for low-loss coupling between polarization-insensitive microwaveguides and single-mode optical fibers," *J. Lightwave Technol.* **21**, pp. 2429–2433, 2003.
32. S. L. Chuang, *Physics of Optoelectronic Devices*, Wiley, New York, 1995.
33. R. Zia, M. D. Selker, P. B. Catrysse, and M. L. Brongersma, "Geometries and materials for subwavelength surface plasmon modes," *J. Opt. Soc. Am. A* **21**, pp. 2442–2446, 2004.